AIAA AVIATION Forum
June 27-July 1, 2022, Chicago, IL & Virtual
AIAA AVIATION 2022 Forum

10.2514/6.2022-3728

A Data-Driven Approach For Real-Time Estimation of Material Properties

Rui Fu *, Sujit Sinha †, Christopher T. Barrow ‡, John F. Maddox §, Jesse B. Hoagg ¶, and Alexandre Martin ‖
University of Kentucky, Lexington, Kentucky, 40506

Modern Thermal Protection Systems (TPS) used for planetary exploration missions often utilize lightweight porous materials as their outer isolating layer. Due to its stochastic nature, such material exhibits a high level of material variability in various properties. Therefore, it is of paramount importance to accurately estimate the uncertainty margin and to understand how material response is affected. In this study, a well-established data-driven algorithm is used to estimate the FiberForm conductivity by using real-time experimental data. By combining the real-time experimental data and a high-fidelity simulation model, the inherent material property is obtained via the proposed method - the retrospective adaptation algorithm. The results also indicate that this methodology is of great potential and can be applied to a wide range of engineering problems, including parameter evaluation, and experimental data processing.

Nomenclature

Δt_{adapt}	=	adaptation time step
η_{adapt}	=	positive integer
Δt	=	computation time step
N	=	number of measurement locations
n	=	adaptation time step
θ	=	adaptation closure coefficient matrix
σ	=	standard deviation (closure coefficient)
$\phi_{m,i}$	=	measurement at the $i^{/textth}$ location
$\phi_{s,i}$	=	simulated value at the $i^{/textth}$ location
ζ	=	performance used to adapt closure coefficient matrix
f	=	feedback vector of simulated results
$M_i(n)$	=	set of square matrices $(\theta \times \theta)$ at each adaptation time step
$N_i(n)$	=	set of matrices $(\theta \times f)$ at each adaptation time step
$L(n)$	=	set of column matrices $(1 \times \theta)$ at each adaptation time step
Q	=	adaptive parameter
ψ	=	column matrix composed of the feedback vector, closure coefficient matrix, and value 1
$\hat{Q}$	=	optimization variable
ζ_r	=	retrospective performance
H_j	=	jth impulse response parameter from θ to ζ
q	=	stacked matrix of adaptive parameter Q
$\hat{q}$	=	stacked matrix of optimization variable $\hat{Q}$
J	=	retrospective cost
Subscripts		
m	=	measurement
s	=	simulated
r	=	retrospective

*Research associate, Mechanical and Aerospace Engineering, AIAA Member.
†Graduate Research Assistant, Mechanical and Aerospace Engineering, AIAA Student Member.
‡Graduate Research Assistant, Mechanical and Aerospace Engineering, AIAA Student Member.
§Associate Professor, Mechanical and Aerospace Engineering, Member AIAA.
¶Professor, Mechanical and Aerospace Engineering.
‖Professor, Mechanical and Aerospace Engineering, Associate Fellow AIAA.

I. Introduction

The intense aerodynamic heating experienced by vehicles during hypersonic atmospheric entry necessitates the use of thermal protection systems (TPS). In recent years, low-density ablative materials have been employed effectively to mitigate the heating experienced by the vehicle through various processes such as charring, pyrolysis gas transport and "surface" ablation [1]. To achieve lower density while maintaining mechanical strength, carbon fiber is used as a substrate matrix for many popular TPS materials, such as phenolic impregnated carbon ablator (PICA). The random nature of stacking or weaving fibers in those materials leads to variability at multiple length scales. Such unpredictability is undesired but unavoidable. At the micro-scale, randomly stacked carbon fibers can form weak locations, such as a small local cavity, that leads to localized thermal and structural loading [2]. At the macro-scale, that variability may lead to non-uniform heating, thus creating a radical temperature gradient within the vehicle [3]. During the ground testing stage, the material variability can lead to incorrect material margin policy [4]. Thus, estimating the variability range of a candidate TPS material at an early stage is crucial.

Due to the lack of test or operational flight data, historical techniques for determining TPS material variability have typically utilized the knowledge and insights of subject matter experts to assign uncertainty values to various TPS aeroheating parameters or components [5]. Uncertainty estimation has also been conducted employing rigorous approaches; however due to computational resource limitations, these studies have not fully achieved the requisite non-linear multivariate analysis [6–8]. The composite aeroheating uncertainty is then determined by employing a worst-on-worst case approach or via a root-sum-square (RSS) approach [9]. The worst-on-worst case approach can be overly conservative, while the RSS approach is only valid for a small number of linearly independent variances[4]. Moreover, if the aeroheating component uncertainties are not properly set, the result can be non-conservative [6].

To address the aforementioned difficulties, presented in this paper is a data-driven adaptive real-time (DART) approach to improve simulation accuracy by calculating and continuously iterating the closure coefficients of a physics model. This approach was originally devised for adaptive control systems [10–12] but was then re-framed to adapt k-ω closure coefficients in turbulence modeling [13, 14]. By utilizing the retrospective cost adaptation (RCA) algorithm, the k-ω closure coefficients are automatically adapted to improve the agreement between the simulated flow field and measured data, which are specified at spatial locations in the flow field. The RCA algorithm finds values for model parameters that minimize the difference between the simulated flow field and measurements over a block of data from the recent past. Then, this "re-optimized" value for the model parameter is used at the next time step. The stability properties of the RCA algorithm are analyzed in Ref. [10].

In contrast to the data-driven approach in Ref. [13], the RCA-RANS k-ω model presented is applicable not only to steady turbulent flows but also to general multiphysics modeling. The RCA algorithm is implemented in combination with a material response solver to model heat conduction and replicate experiments. This approach will automatically retrieve the value of material properties and drive the simulation results to match the experiments. In the following sections, the mathematical framework of the code will be reviewed along with the the details of the data-driven algorithm. Details of the experiment design and setup will also be presented.

II. Numerical Framework and Formulations

A. Numerical framework

The material response and Retrospective adaptation codes have both been developed within the framework of the Kentucky Aerothermodynamic and Thermal-response System (KATS) [15]. KATS is a multiphysics modeling framework, capable of analyzing hypersonic flows [16], the trajectory of spallation particles [17], and low-speed turbulent flows [13]. It is also a universal solver for fluid-solid-interaction modeling [18], material response [15] and structural response as well as thermo-mechanical coupling problems [19, 20]. In KATS, a universal Finite Volume Method framework is used, with second-order accuracy in space and first-order accuracy in time. More details of the framework and governing equations can be found in the mentioned references.

B. Definition of a black-box model

To help better understanding the mathematics and framework, a very general black-box model will be introduced. A black-box model can be described as an input-output system with a general function $\mathbf{F}$, which can be treated as a data processor, or a solver, as

$$\mathbf{\Phi_s^t} = \mathbf{F}(\mathbf{\Phi_s^{t-1}}, \theta), \tag{1}$$

where $\mathbf{\Phi}_\mathbf{s}^\mathbf{t}$ is the primitive variable set of this model output at the current time step. The subscript $_s$ denotes that this variable is the result of a simulation, or a model, comparing to experimental measurements. The θ can be a combination of any model parameters, such as boundary conditions, model geometric information, material properties and even some hyper-parameter such as time step size.

C. Retrospective cost adaptation algorithm

Experimental data consisting of N temperature measurements at specified locations are required for the retrospective cost adaptation (RCA) algorithm. Within the context of this algorithm, the term *measurement* is defined as *a priori* information about the temperature distribution at N locations. The measurements and the associated simulated values are specified by

$$\mathbf{\Phi}_m \triangleq \begin{bmatrix} \phi_{m,1}(n) \\ \vdots \\ \phi_{m,N}(n) \end{bmatrix} \in \mathbb{R}^{l_\Phi} \tag{2}$$

$$\mathbf{\Phi}_s \triangleq \begin{bmatrix} \phi_{s,1}(n) \\ \vdots \\ \phi_{s,N}(n) \end{bmatrix} \in \mathbb{R}^{l_\Phi} \tag{3}$$

where $\phi_{m,i}(n) \in \mathbb{R}^{l_i}$ is the measurement value at the i^{th} location (matrix of real numbers length N), $\phi_{s,i}(n) \in \mathbb{R}^{l_i}$ is the simulated value at the i^{th} location (matrix real numbers length N), $n \in \mathbb{N}$, $i = 1, \ldots, N$, N is the number of measurement locations, and $l_\Phi \triangleq \sum_{i=1}^{N} l_i$.

To adapt the closure coefficients, $\theta(n)$, *performance* is defined as

$$\zeta(n) \triangleq \mathbf{\Phi}_s(n) - \mathbf{\Phi}_m(n) \tag{4}$$

The external driver or feedback for $\theta(n)$ is a vector of simulated field output (e.g. temperature), which is denoted by $f(n) \in \mathbb{R}^{l_f}$. Therefore, for all $n \in \mathbb{N}$, the closure coefficients to be stated as an auto-regressive moving-average (ARMA) model with feed-forward bias as given by

$$\theta(n) = \sum_{i=1}^{n_c} M_i(n)\theta(n-i) + \sum_{i=1}^{n_c} N_i(n) f(n-i) + L(n) \tag{5}$$

where n_c is a positive integer (time step), $M_i(n) \in \mathbb{R}^{l_\theta \times l_\theta}$ is a set of square matrices $(\theta \times \theta)$ at each adaptation time step, $N_i(n) \in \mathbb{R}^{l_\theta \times l_f}$ is a set of matrices $(\theta \times f)$ at each adaptation time step, and $L(n) \in \mathbb{R}^{l_\theta}$ is a set of column matrices $(1 \times \theta)$ at each adaptation time step.

Note that $M_i(n)$ is the auto-regressive parameter as a function of time, $N_i(n)$ is the moving average as a function of time, and $L(n)$ is the feed-forward bias as a function of time and these values are updated according to the adaptive law presented herein. The ARMA model is initialized with $M_i(0) = 0_\theta \times l_\theta$, $N_i(0) = 0_\theta \times l_f$, and $L(0) = \in \mathbb{R}^l_\theta$. As an example, $\theta(0) = L(0)$ can be the closure coefficients as proposed in Reference [21].

The ARMA model, Eq. (5), can be rewritten as

$$\theta(n) = Q(n)\psi(n) \tag{6}$$

where $Q(n)$ is the adaptive parameter given by

$$Q(n) = [N_1(n) \cdots N_{n_c}(n) \;\; M_1(n) \cdots M_{n_c}(n) \;\; L(n)] \in \mathbb{R}^{l_\theta \times (n_c(l_f + l_\theta)+1)} \tag{7}$$

and,

$$\psi(n) \triangleq \begin{bmatrix} f(n-1) \\ \vdots \\ f(n-n_c) \\ \theta(n-1) \\ \vdots \\ \theta(n-n_c) \\ 1 \end{bmatrix} \in \mathbb{R}^{(n_c(l_f+l_\theta)+1)} \tag{8}$$

Next, an update equation for $Q(n)$, or the adaptation parameters, are expressed by setting $\hat{Q}$ as the optimization variable and defining *retrospective performance* as

$$\hat{\zeta}_r(\hat{Q}, n) \triangleq \zeta(n) + \sum_{j=1}^{n_r} H_j[\hat{Q} - Q(n-j)]\psi(n-j) \tag{9}$$

where $\hat{Q} \in \mathbb{R}^{l_\theta \times (n_c(l_f+l_\theta)+1)}$ and $\hat{Q}$ is Q initially, n_r is a positive integer, $H_j \in \mathbb{R}^{l_\Phi \times l_\theta}$ is the j^{th} impulse-response parameter from θ to ζ.

The retrospective performance is calculated based on the true performance by assuming that the optimization variable, $\hat{Q}$, was employed in place of prior adaptive parameters $Q(n), \ldots, Q(n-n_r)$. As a result, the retrospective performance serves as a proxy for the actual performance. The adaptive parameter is deemed to have converged when $Q(n)$ is constant, indicating that $Q(n-i) \equiv Q(n)$ in which case $\hat{\zeta}(Q(n),(n)) \equiv \zeta(n)$ as an outcome of the retrospective performance equation.

Recalling that vec X is the vector created by stacking the columns of matrix X, the following two stack matrices can be defined

$$q(n) \triangleq \text{vec}\, Q(n) \in \mathbb{R}^{l_q} \tag{10}$$

$$\hat{q}(n) \triangleq \text{vec}\, \hat{Q}(n) \in \mathbb{R}^{l_q} \tag{11}$$

where $l_q \triangleq l_\theta(n_c(l_f + l_\theta) + 1)$.

Therefore, retrospective performance can be rewritten as

$$\hat{\zeta}_r(\hat{q}, n) = \zeta(n) + \sum_{j=0}^{n_r} \psi^{\mathrm{T}}(n-j) \otimes H_j\hat{q} - \sum_{j=0}^{n_r} H_j\theta(n-j) \tag{12}$$

or,

$$\hat{\zeta}_r(\hat{q}, n) = \zeta(n) + \Psi^{\mathrm{T}}(n)\hat{q} - \sum_{j=0}^{n_r} H_j\theta(n-j) \tag{13}$$

where $\otimes$ - is the Kronecker product and,

$$\Psi(n) \triangleq \sum_{j=0}^{n_r} \psi(n-j) \otimes H_j^{\mathrm{T}} \in \mathbb{R}^{l_q \times l_\Phi} \tag{14}$$

Next, the retrospective cost is established from

$$J(\hat{q}, n) \triangleq \sum_{i=0}^{n} \hat{\zeta}_r^{\mathrm{T}}(\hat{q}, i)\hat{\zeta}_r(\hat{q}, i) + [\hat{q} - q(0)]^{\mathrm{T}}\, \Gamma[\hat{q} - q(0)] \tag{15}$$

Note that $\Gamma \in \mathbb{R}^{l_q \times l_q}$ is symmetric and positive definite, meaning $A_n = A_n^{\mathrm{T}}$, and all eigenvalues are positive. Then for each $n \in \mathbb{N}$, the unique global minimizer of the retrospective cost J is given by a recursive least squares algorithm as follows

$$q(n+1) = q(n) - P(n)\Psi(n)\Omega^{-1}(n)\zeta_r(n) \tag{16}$$

where,

$$P(n+1) = P(n) - P(n)\Psi(n)\Omega^{-1}(n)\Psi^{\mathrm{T}}(n)P(n) \tag{17}$$

By defining the following two parameters

$$\zeta_r(n) \triangleq \hat{\zeta}_r(q(n), n) + \Psi^{\mathrm{T}}(n)q(n) - \sum_{j=0}^{n_r} H_j\theta(n-j) \tag{18}$$

$$\Omega(n) \triangleq I_{l_{|\Phi}} + \Psi^{\mathrm{T}}(n)P(n)\Psi(n) \tag{19}$$

and, $P(0) = \Gamma^{-1}$. Then $Q(n+1)$ is computed from

$$Q(n+1) = \text{vec}^{-1} q(n+1) \in \mathbb{R}^{l_\theta \times (n_c(l_f+l_\theta)+1)} \tag{20}$$

where, vec^{-1} is the inverse operator, meaning $\text{vec}^{-1}\text{vec}\, Q(n) = Q(n)$. Also, the equations (16) and (19) are a recursive, least-squares algorithm.

Parameter drift is a known issue in adaptation programs [22], since in reality, the RCA algorithm will not drive the performance parameter, $\zeta(n)$, exactly to zero. Consequently, there will be a residual difference between the measurement values, $\Phi_m(n)$, and the simulation values, $\Phi_s(n)$, for a variety of reasons including noise in the measurements, noise in the numerics, and the reality that simulation models do not match experimental data perfectly. So, since $\zeta(n)$ does not converge exactly to zero, then per Eq. 16, $\zeta(n)$ will continue to adapt, which will cause the closure coefficients, $\theta(n)$, to continue to adapt, since $\zeta(n)$ is used to update $\theta(n)$. Therefore, a deadzone approach is introduced to eliminate parameter drift. A *modified retrospective* performance is defined as:

$$\zeta_r'(n) \triangleq \begin{cases} \zeta_r(n), & \text{if } d(n) \geq \epsilon_0, \\ 0, & \text{if } d(n) < \epsilon_0, \end{cases} \tag{21}$$

where,

$$d(n) \triangleq \sum_{i=0}^{N_d} \left| \|\zeta_r(n-i)\|^2 - \|\zeta_r - i - 1\|^2 \right| \tag{22}$$

where $\epsilon_0 > 0$, and N_d is a nonnegative number.

In summary, the RCA algorithm employed in the code-base consists of equations (6), (14), (17) through (22) and

$$q(n+1) = q(n) - P(n)\Psi(n)\Omega^{-1}(n)\zeta_r'(n) \tag{23}$$

III. Adaptation Demonstration Case

To illustrate the implementation details and verify the performance of the developed adaptive algorithm, an adaptation test case is presented. A first-order differential equation system is chosen based on its simplicity,

$$\boldsymbol{X^t} = \mathbf{A}\boldsymbol{X^{t-1}} + \mathbf{B}\theta \tag{24}$$

The differential function output a value, $\boldsymbol{X^t}$, based on its previous value, $\boldsymbol{X^{t-1}}$, and some constant parameters, $\mathbf{A}$, $\mathbf{B}$ and θ. With respect to Eq. 1, the $\boldsymbol{X^t} = \mathbf{\Phi_s^t}$. In this case, those terms are vectorized and set as

$$\boldsymbol{X} = \begin{pmatrix} x_1 \\ x_2 \\ x_3 \\ x_4 \end{pmatrix}, \qquad \mathbf{A} = \begin{pmatrix} -0.5 \\ 0.5 \\ -0.5 \\ 0.5 \end{pmatrix}, \qquad \mathbf{B} = \begin{pmatrix} 0.5 \\ -0.5 \\ -0.5 \\ 0.5 \end{pmatrix}, \qquad \theta = \begin{pmatrix} \theta_1 \\ \theta_2 \\ \theta_3 \\ \theta_4 \end{pmatrix} = \begin{pmatrix} 0.5 \\ 0.5 \\ 0.5 \\ 0.5 \end{pmatrix}. \tag{25}$$

By using an initial value of $\boldsymbol{X}^0 = (0, 0, 0, 0)^T$ and a simple forward time stepping, the solution can quickly reach steady-state, shown in Fig. 1a. It can be observed that the solution is $\boldsymbol{X}^0 = (0.1666, -0.5, -0.1666, 0.5)^T$ at time step around 10. Once the solution reaches steady-state, the impulse can be applied to θ. To do so, the value of each θ is increased by 1 at the current time step and then changed back to its original value. This process can be viewed in Fig. 1b, where each θ has been impulsed at a certain time interval. It should be noted that once the impulse is applied, the next impulse must wait until the solution reaches steady-state again. Due to a sudden change in θ, the solution shows fluctuations in $\boldsymbol{X}$, shown in Fig. 1a. Since each equation is independent, the changes in $\boldsymbol{X}$ only have a dependence in the corresponding θ.

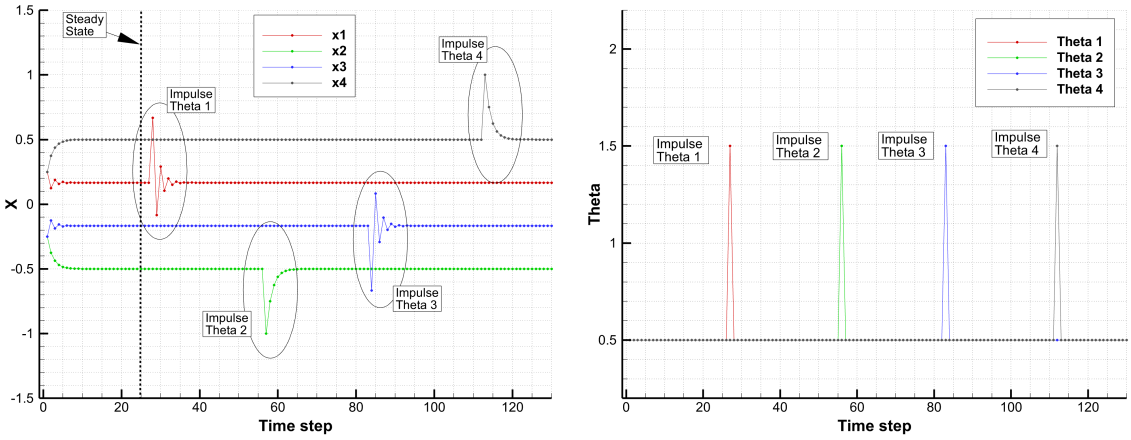

(a) Evolution of the solution $\boldsymbol{X}$

(b) Impulse of the θ

Fig. 1 Demonstration test case of the adaptation algorithm.

To isolate the impacts of the impulses of θ on the equation system, the values of the changing $\boldsymbol{X}$ are subtracted by its steady-state values and then stored. Figure 2 shows the values of such operations. For each subfigure, one item of θ is impulsed and the absolute changes of $\boldsymbol{X}$ are recorded. It can be seen that for all cases, the solution quickly converges back to its original values. The patterns in Figs. 2a and 2c are similar since the values are fluctuating around 0; while Figs. 2b and 2d show a mono-directional decay to 0. Additionally, it can be clearly seen that each item of θ only affects its corresponding $\boldsymbol{X}$.

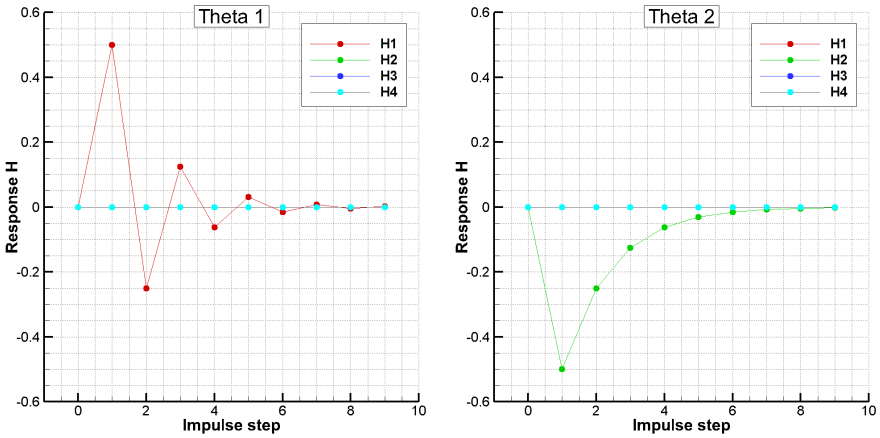

(a) Response of the solution to θ_1

(b) Response of the solution to θ_2

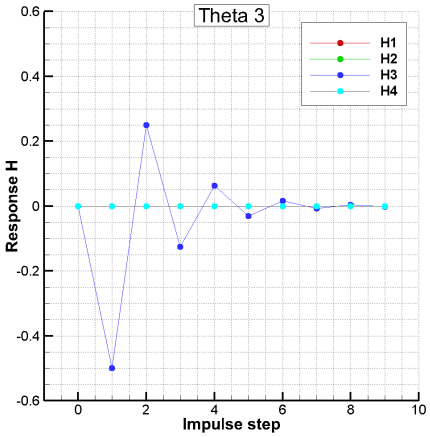

(c) Response of the solution to θ_3

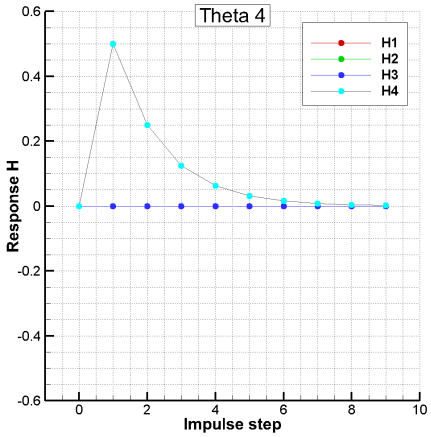

(d) Response of the solution to θ_4

Fig. 2 Response of the impulse of the equation system.

To test the performance of the adaptation algorithm, the model parameter θ is set to be $\theta = (\mathbf{0.2}, \mathbf{0.2}, \mathbf{0.2}, \mathbf{0.2})$, and the measured solution is generated by setting $\theta = (\mathbf{0.3}, \mathbf{0.3}, \mathbf{0.3}, \mathbf{0.3})$. Figure 3a shows that the overall solution reaches a steady state at time step 25. At time step 26, the adaptation starts. It can be seen that the values of each $\boldsymbol{X}$ start to deviate from the steady-state solution, then quickly converges to new values, which are the measured values. Figure 3b presents the evolution of θ. All four components of θ starts at 0.2. At step 26, the values rapidly increase in two steps and fall back into a stable curve. It should be noted that all components have been adapted at the same time, during which the θ_1 and θ_3 share the same pattern of adaptation. This is because the responses of the impulse for these two parameters deliver the same pattern, which has been discussed before. Another point is that the overall adaptation process is very effective and quick - θ quickly converges to the known measured value in less than 75 adaptation steps. To better compare the fitting wellness of the results, an error is defined as,

$$L_2 \text{ error} = \sqrt{\sum_{n=0}^{N} (\Phi_s(n) - \Phi_m(n))^2} \tag{26}$$

The L_2 error is presented in Fig. 3c. The solution residual reaches 0 very quickly; after adaptation starts, it jumps in a few steps, and then rapidly falls back to 0 again. The performance maintains a value when the solution reaches a steady state. Once the adaptation starts, the error quickly decreases in a few steps and eventually reaches 0.

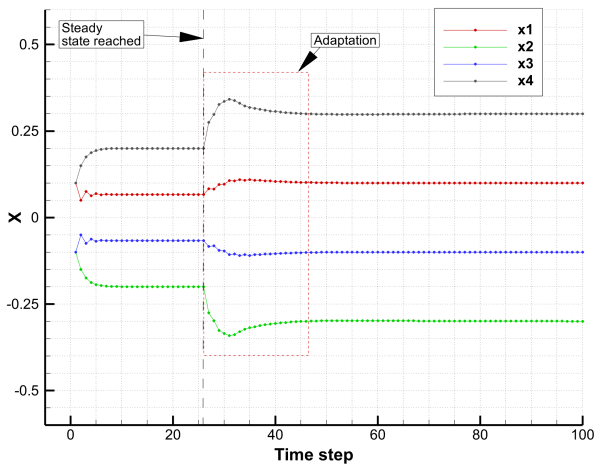

(a) Adaptation evolution of $\boldsymbol{X}$

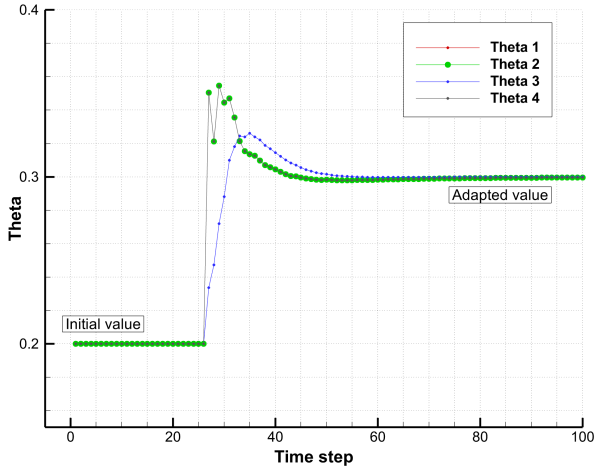

(b) Adaptation evolution of θ

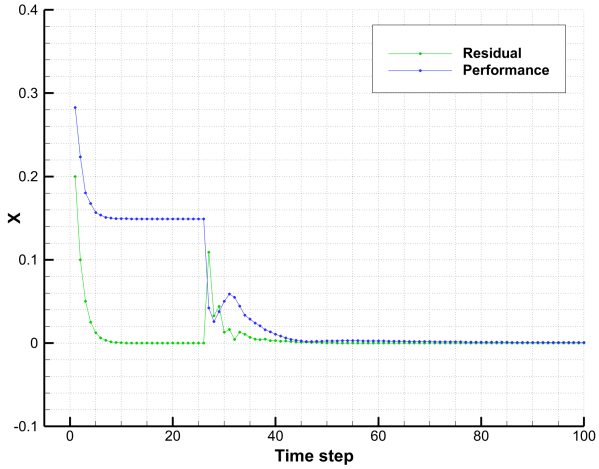

(c) Evolution of the residual and performance

Fig. 3 Adaptation of the first-order differential equation system.

In this case, the adaptation works very well, with the performance reaching 0 after tens of steps and all the θ have been adapted to exact values. One of the reasons is that the first-order differential equations are very simple and highly linear. Secondly, although it is a four-equation system, each equation is independent so there is no interaction between θ. This test case demonstrates how the developed RCA algorithm works and the benefits it can provide for parameter discovery processes using measured data.

IV. Experimental Setup

The experiment used to collect data is a comparative cut-bar apparatus as described in ASTM D5470 [23]. The experiment is housed inside a thermal vacuum chamber such that the pressure and atmospheric composition that the sample material is exposed to can be varied. Further details on the experiment can be found in Barrow et al. [24].

A. Experimental setup and layout

A diagram of the experimental setup is given in Figure 4. Heat is generated by resistance heaters embedded in a copper heating block. The heat flows through a 0.0254 m (1 in) diameter top metering bar where the temperature gradient is measured through five thermocouples spaced 0.0127 m (0.5 in) apart. The sample is placed between the two metering bars and heat flows through the sample into the bottom metering bar with a temperature gradient measured by embedded thermocouples mirroring the top bar. The location of the thermocouples and sample are illustrated in

Figure 5.

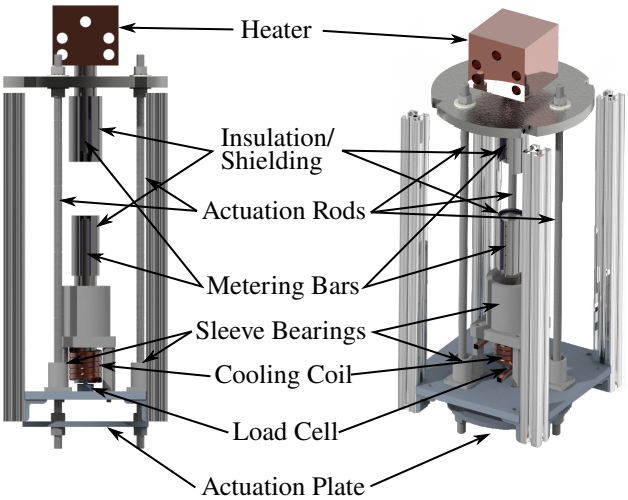

Fig. 4 Experimental Assembly

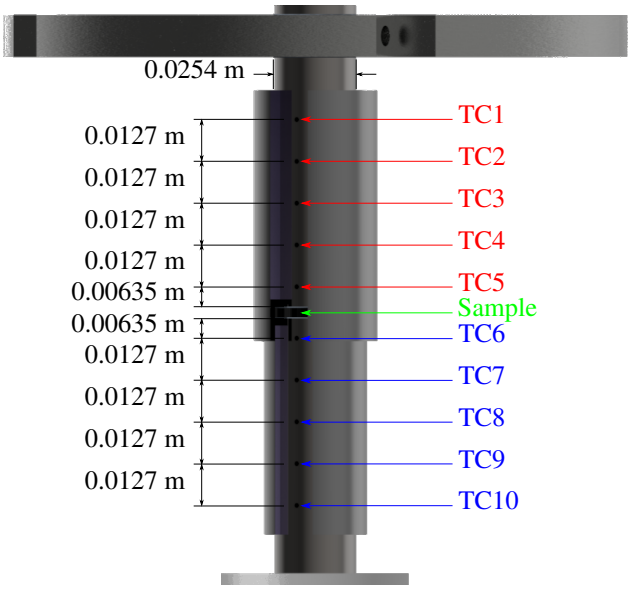

Fig. 5 Thermocouple and sample locations in experimental assembly

Heat is removed through a cooling coil utilizing either water or liquid nitrogen, allowing for variable control of sample temperature. Insulation is wrapped around the metering bars along with radiation shielding that acts to create a baffling region around the sample, retaining heat and reducing losses from the metering bars and sample. The top bar assembly position is controlled by a linear actuator that sits below the experimental assembly. With the coupling of a rotary encoder and load cell, the load and strain placed on the sample can be controlled to ensure consistent interfacial resistance between the sample and metering bars which can be separated during data analysis.

B. Data acquisition

The primary data collected during the experiment is temperatures in the metering bar. Type K thermocouples are embedded in the center of the metering bar, which are monitored by a data acquisition card that polls the thermocouples every second. The linear actuator and load cell are monitored to ensure a consistent load is being applied to the sample. The vacuum chamber pressure is monitored with a Pirani gauge.

C. Data set

In this study, three experimental case results were selected. Key results are summarized in Table 1. The sample names indicate the material, FiberForm, and relative sample length. ΔT is the temperature difference across the sample. It should also be noted that the effective conductivity contains the contacting resistance between the sample and the metering bar. Therefore, the intrinsic value of the FiberForm conductivity should be higher than the effective conductivity.

Table 1 Experimental results on FiberForm

Sample name	Length, in	ΔT, K	Effective conductivity, W/m·K
FF-2	0.145	108.66	0.570
FF-4	0.290	115.44	0.694
FF-long	0.435	146.78	0.795

Figure 6 shows the final temperature distribution of each case. It can be seen that as the sample length becomes longer, the resultant temperature difference increases.

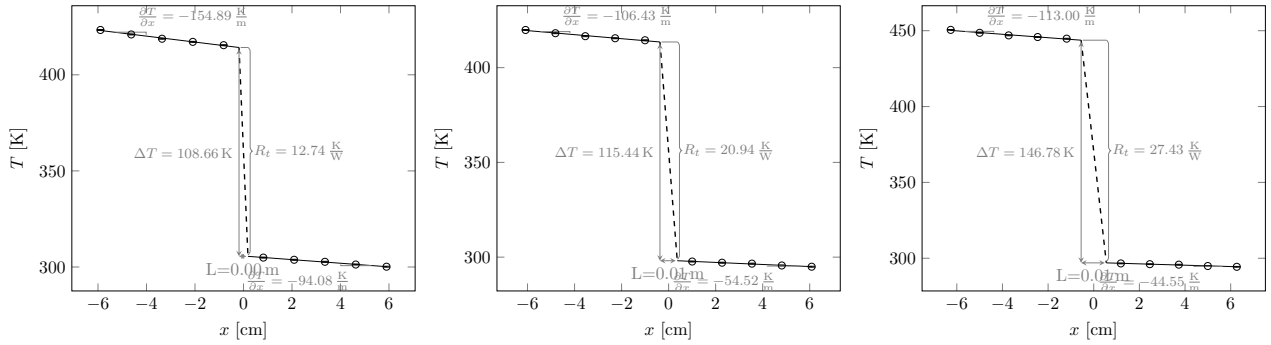

(a) FF-2 (b) FF-4 (c) FF-long

Fig. 6 Steady-state temperature distribution of the experiments.

V. Results

In this section, replicate modeling cases will be presented to show how temperature results and setup are obtained. To capture the physics, an energy conservation equation is solved in a Finite Volume Method framework, without a source term,

$$\frac{\partial}{\partial t}\int_V \rho c_p T\, dV = \oint_A k\nabla T \cdot \boldsymbol{n}\, dA. \tag{27}$$

where t is time, V is cell volume, ρ is density, c_p is heat capacity, T is the primitive variable, temperature, A is the local cell face area, k is the thermal conductivity, and $\boldsymbol{n}$ is the face normal vector.

A. Boundary conditions and grid

Figure 7 displays the computational grid and boundary conditions of this case. To capture the full physics of the experiment, the geometries of both the metering bar and sample are constructed as a quarter cylinder with the same dimensions. The mesh is extensively refined for the sample so that the variability of the material properties can be implemented. At the left front of the metering bar, a fixed temperature from TC1 is applied; and at the right end, a fixed temperature from TC10 is applied. The two inner surfaces are symmetric, while the outer surface of the cylinder is applied with an advection cooling heat flux. The simulation is setup to run until the steady-state solution is reached. For each data set, three different grids are created to match the sample length and the boundary conditions.

Figure 8 displays the density contour of both the metering bar and the FiberForm sample. Firstly, the material model assumes that there is no thermal resistance at the interface between the sample and the metering bar. Therefore the value

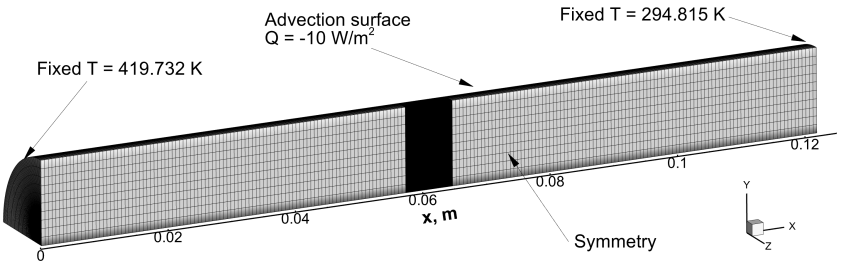

Fig. 7 Boundary conditions and computational grid for data set FF-4

of the conductivity used on that face is the average of the metering bar material and the sample. Then, the interface resistance will be modeled as a surface with a very low conductivity value.

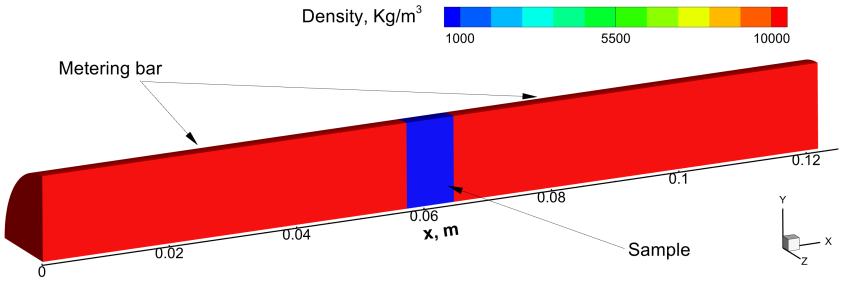

Fig. 8 Density of the metering bar and sample.

The material properties of the metering bar are known and assumed to be isotropic and constant. The detailed values are presented in figure 9.

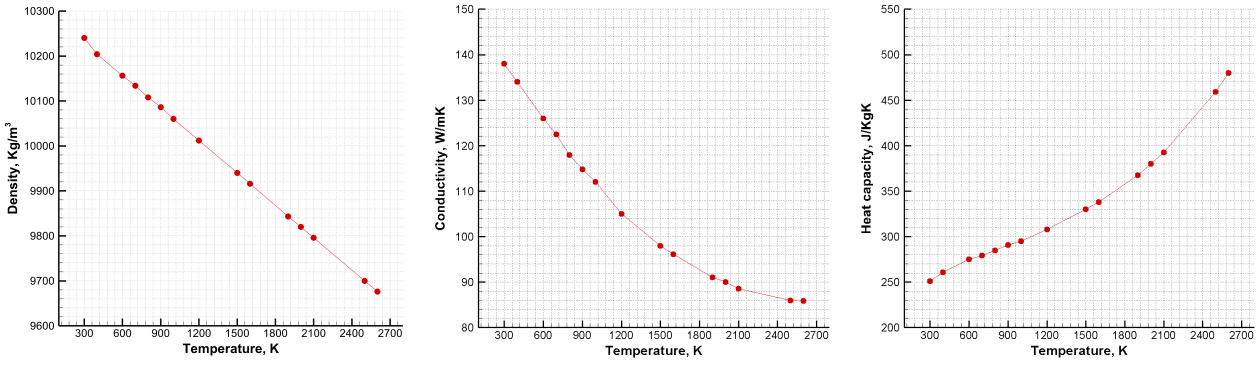

(a) Metering bar density (b) Metering bar thermal conductivity (c) Metering bar heat capacity

Fig. 9 Metering bar material properties.

The material properties of FiberForm are given in Table 2. In this study, all properties are assumed to isotropic and constants. The effective conductivity, which includes the interfacial resistance, is the target parameter. Thus, the value of 0.2 $\mathrm{W/m \cdot K}$ is an initial guess, which will be adapted to seek a fitted value.

B. Modeling results

Figure 10a presents the steady-state temperature of the entire domain. It can be seen that the left metering bar is in a high-temperature region. The sample, due to its very low conductivity, has effectively cut the energy conduction.

Table 2 Material properties of FiberForm

Density	Specific heat	Effective conductivity (Initial guess)
200, kg/m^3	200, J/kg·K	0.2, W/m·K

Therefore, the right-part bar exhibits a low-temperature region. Figure 10b shows the temperature results extracted at the center-line. Since the material is assumed to be constant and isotropic, the temperature is linear in both the metering bar and sample region. Also due to the sharp differences in material properties, the slopes in these regions are different, as would be expected. The FiberForm has a very low conductivity, which leads to a sharp temperature gradient between the metering bars. Consequently, the sample acts as a thermal barrier, slowing down the energy propagation. Figure 10c presents the temperature evolution of the 8 thermocouples. It can be seen that the simulation reaches steady-state quickly around 200 seconds.

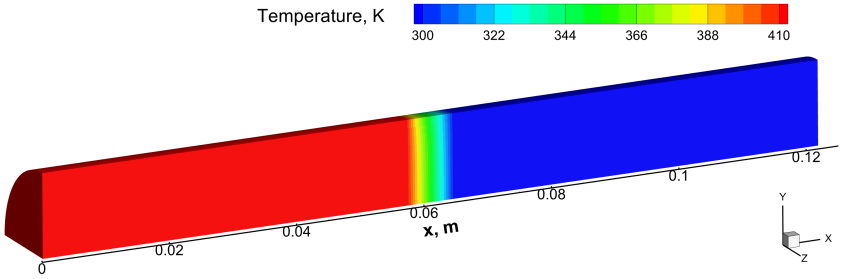

(a) Steady-state temperature distribution over the whole domain.

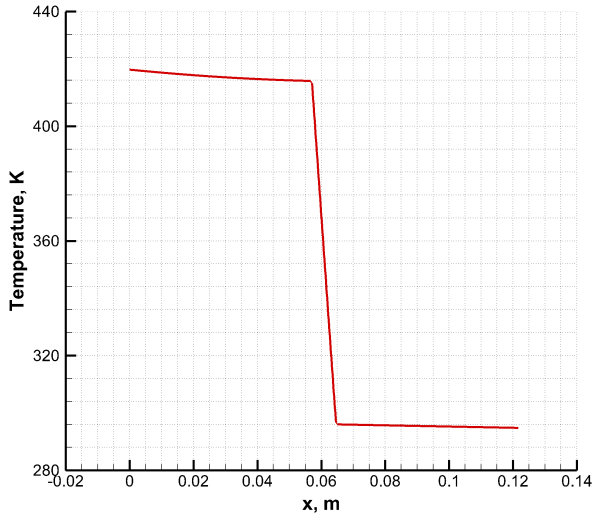

(b) Extracted results at center-line

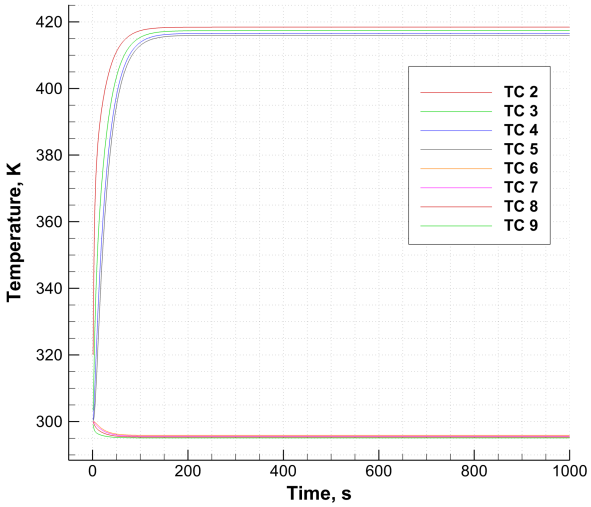

(c) thermocouple results

Fig. 10 Temperature results for the experimental case FF-4.

C. Adaptation of conductivity

To apply the RCA algorithm, the responses of the thermocouples are needed. To obtain the response, the effective conductivity of the sample has been increased by 1 in one time step and changed back to the original at the following step. Figure 11a shows the responses of the temperature in the form of absolute values. It can be seen that as TC 5 and TC 6 are the closest to the sample, they show large fluctuations immediately. In about 50 time steps, the system stabilized and returned to the steady-state solution. Figure 11b presents the adaptation process of the effective conductivity. The initial guess is 0.2 W/m·K. After 200 time steps, the adaptation starts to work. It can be observed that the algorithm moves the value up and down in a range of [0~1], and it fluctuates within this interval in approximately 100 steps. After that, the

amplitude decays and gradually falls into a smaller and smaller range. After about 1,000 steps, the adapted conductivity value is achieved at approximately 0.523 W/m·K. Figure 11c shows the solution residual and performance history over time. It can be seen that at the beginning, the solution reaches a steady state, while the performance maintains a relatively high level. Once the adaptation begins to work, the performance decreases rapidly. The error of measurements and simulation results reaches a low value when the solution reaches steady-state again. The error of the RCA algorithm does not necessarily decrease to zero in the adaptation process since other factors could also affect the thermocouple readings.

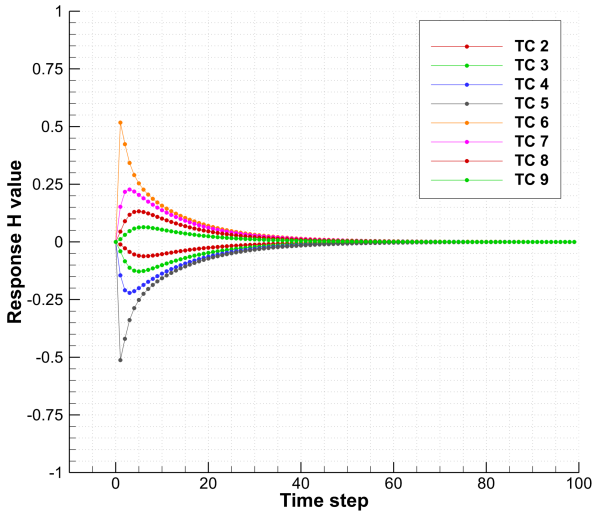

(a) Responses for 8 thermocouple locations.

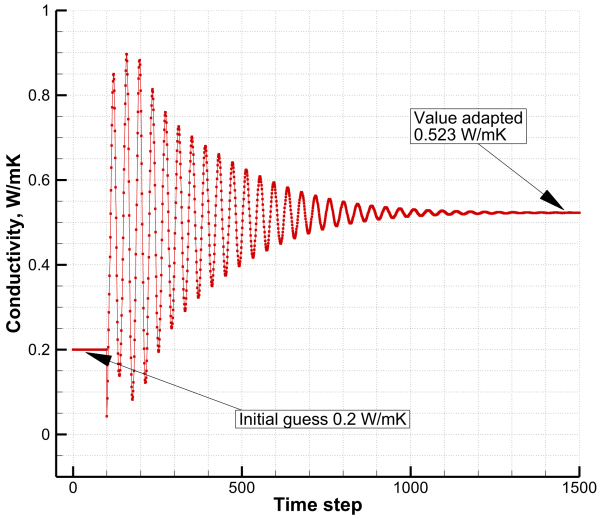

(b) Adaptation process of conductivity

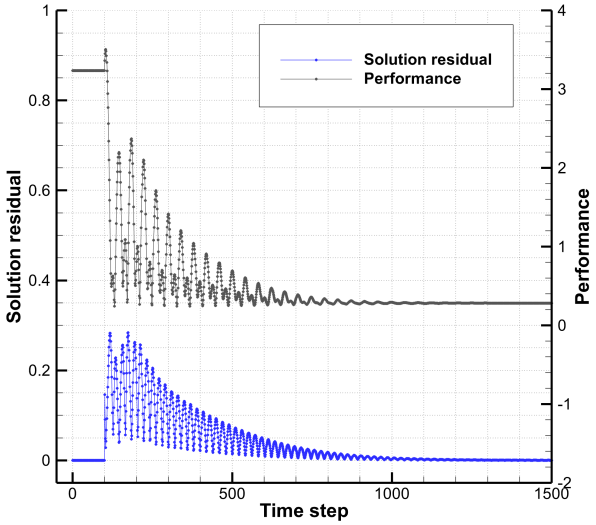

(c) Simulation residual and adaptation performance.

Fig. 11 Adaptation results for data set FF-4.

The same process has been applied to the experiments FF-2 and FF-long. Figure 12a and 12c shows the response H of the sample FF-2 and FF-long. It can be seen that there are some differences in the amplitude, but they do share the same pattern compared with the FF-4. Figure 12b and 12d presents the adaptation process of these two cases. For FF-2, the adaptation process is more intense and much shorter than FF-long. The adapted value starts from 0.2 W/m·K, and quickly reaches 1.45 W/m·K, then it falls back and decays to a stable value. For FF-long, the adaptation takes more time and reaches a lower value of 0.461 W/m·K.

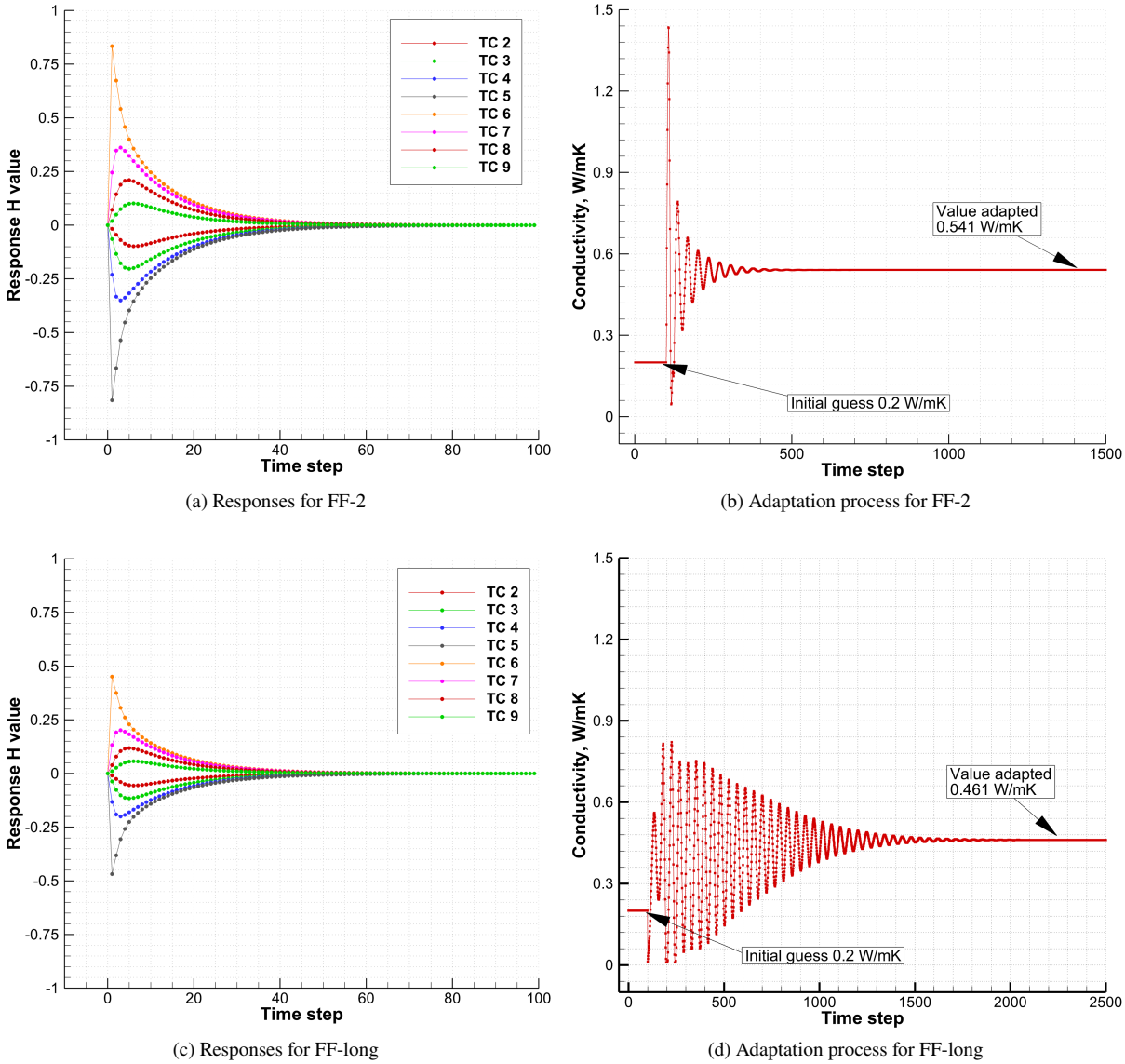

(a) Responses for FF-2

(b) Adaptation process for FF-2

(c) Responses for FF-long

(d) Adaptation process for FF-long

Fig. 12 Adaptation results for data set FF-2 and FF-long.

Table 3 shows a summary of the adapted effective conductivity compared with the experimental results. The adapted effective conductivity shows some degree of similarity to the experimental results. At least the values are of the same order of magnitude. It is, however, not promising to see that the adaptation fails to catch the increasing pattern as the sample length increases. Two main reasons may cause this discrepancy. The first one is the advection heat flux. Currently, it is modeled as negative heat flux, with a constant value over the entire outer surface. And the actual value of this cooling flux in the experiments is very hard to quantify. The second one is the contacting thermal resistance. FiberForm is a highly porous material. Different samples with different cutting locations from a bulk material may lead to a very different surface roughness of the cut surface. Therefore, the contacting thermal resistance for each experiment may differ.

D. Evaluation of the influential factors - advection strength

The results indicate the developed RCA algorithm can be used as a parameter-fitting method to explore material properties. It thus can be used as a tool to evaluate how environmental conditions affect the results. Figure 13 shows the results by varying the magnitude of advection. Each point is a single run of FF-4, with different values of advection flux

Table 3 Comparison of the effective conductivity

Name	Adaptation value, W/m·K	Experimental value, W/m·K
FF-2	0.523	0.570
FF-4	0.541	0.694
FF-long	0.461	0.795

applied on the outer surface. It can be observed that when advection is strong, the algorithm will deliver a smaller conductivity. As the advection becomes smaller, the value of conductivity increases linearly and reaches a maximum when advection is around -200 W/m^2. This behavior can also be explained in an energy balance perspective of view - if stronger advection occurs during the experiment, to maintain the same temperature difference, a lower conductivity of the sample would be required.

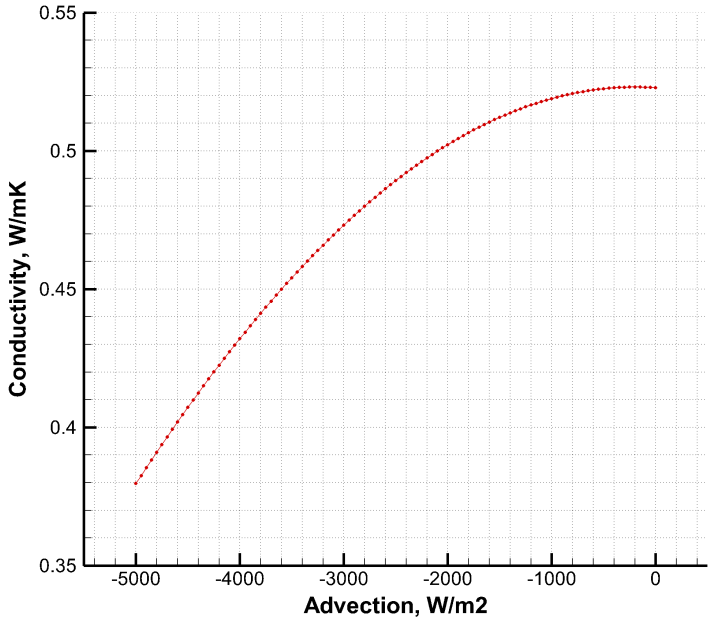

Fig. 13 Advection influences on adapted conductivity value for FF-4.

E. Evaluation of the influential factors - contacting thermal resistance

Based on the previous results, the RCA algorithm can be used as a tool to evaluate how one environmental condition affects the targeted parameter. In this case, the model will be further refined to include the contacting resistance. The contacting resistance, also known as interfacial thermal resistance, is due to the surface roughness of the sample and the metering bar. During the experiment, asperities on the contacting surfaces lead to localized voids that inhibit heat transfer. For each experimental test, the roughness of the sample may vary because of the cutting location, pore distribution, and forces exerted on the metering bar. It difficult to quantify the true contacting thermal resistance between the sample and the metering bar.

Based on Eq. 27, one way to model the contacting thermal resistance is to change the k on the interface to a low value so that it becomes harder for energy to pass. To fully discover the impact of the contacting resistance, the $k_{\text{interfacial}}$ was sampled from [0.05~1.05] W/m·K, with a interval value of 0.01. Therefore, for each sample, 101 cases are performed. Figure 14 presents the adapted conductivity value for all the cases. For all samples, the sample conductivity discovered by the RCA decreases as the interfacial thermal resistance increases. For FF-2, because of the shortest length, the adapted conductivity is very sensitive to interfacial resistance. As the $k_{\text{interfacial}}$ becomes smaller, the adapted conductivity increases exponentially and reaches an unrealistically high value. For FF-4 and FF-long, as the sample length is increased, the adaptation value becomes less sensitive. Because for each test, the sample conductivity is a constant, the results can also be used to evaluate the range of the targeting parameter by assuming the only changing

parameter is the interface conductivity for all three tests. Comparing three curves, it can be observed that the overlapping range, from [0.5~0.9], can be inferred as the intrinsic value of the FiberForm sample.

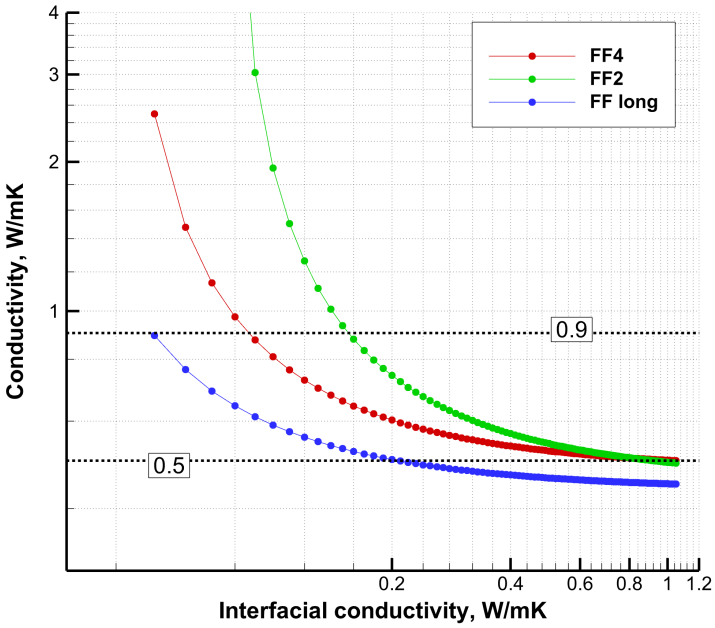

Fig. 14 Influences of interfacial contacting thermal resistance on sample conductivity

F. Real-time property inference

Figure 15 shows the entire history data of the 10 thermal couples. In order to reach a steady-state solution, the experiment lasts about 7.7 hours, which is not including the time spent on the cooling process. Near the end of the experiment, it is also not very easy to call exactly if a steady-state is reached. It is notable that at the first 10,000 seconds, the rate change of the temperature is much larger than the rest of the time, for all the thermal couples. Thus, the question raises - is there a way to discover the conductivity much earlier, during the data richness period, than the end of experiment? It is clear that at early stage, the temperature difference between the metering bar is a dynamic value - it increases as the metering bar and sample reaches a steady-state. At t = 3000 s, the temperature differences is approximately 88.15 K. Apparently, this value cannot be used to calculate the effective conductivity.

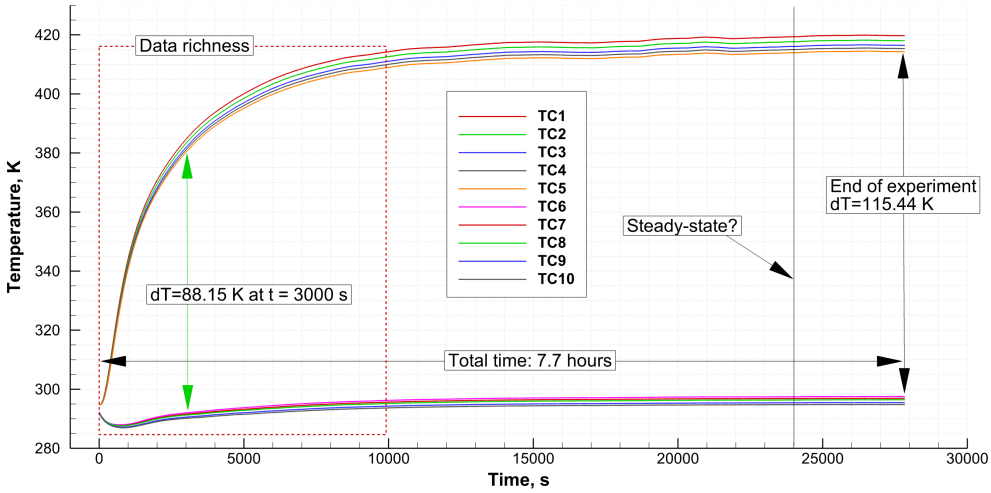

Fig. 15 Temperature measurements of all time for case FF-4.

Figure 16 shows the application of the developed RCA algorithm to discover the conductivity using the real-time temperature measurements. The red line shows the evolution of the adapted conductivity value. Like the previous case, an initial value of 0.2 $W/m{\cdot}$K is used. The adapted value quickly drops to the lower bound, which is set to be 0.001 $W/m{\cdot}$K. And followed by a rapid increasing to about 0.55 $W/m{\cdot}$K. It is very surprising to see that at as early as $t = 1000$ s, the solution starts to show some degree of convergence. As shown in the figure, during $t \simeq [1000, 4000]$ s, the average of adapted value is 0.564 $W/m{\cdot}$K, with a standard deviation of 0.01. It should be noted that even at $t = 4000$ s, as shown in Fig. 15, the thermal couple readings are still increasing rapidly and very far from the steady-state solution. The adaptation keeps working - the adaptation value fluctuates around an averaged value of 0.555. This is because the measurement contains noises and disturbance from the environment. At the end of the experiment, the adaptation uses the last points as steady-state and obtained a value of 0.553 $W/m{\cdot}$K. The error also indicates that at the very early stage, the algorithm adapts the conductivity of the sample to match the measurements very well. The error never exceeds one after approximately $t = 500$ s.

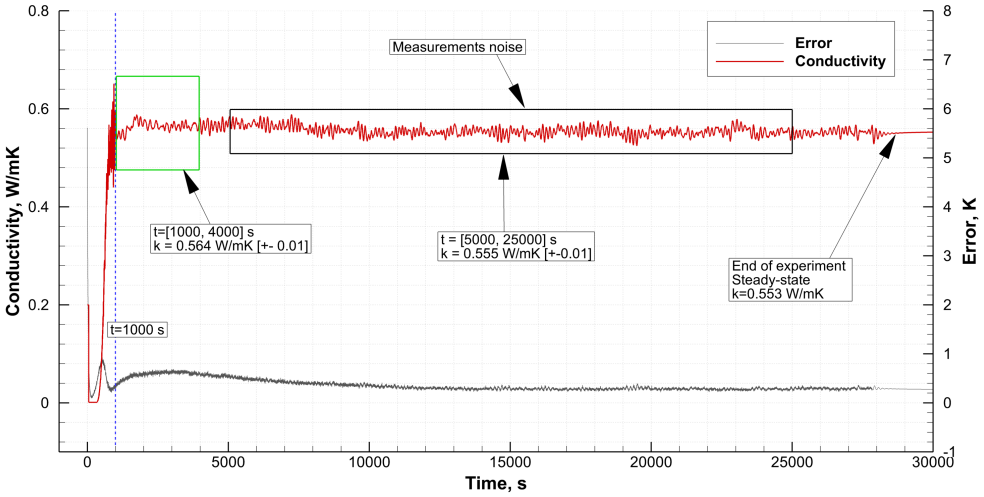

Fig. 16 Real-time adaptation results for case FF-4.

The significance of the real-time adaptation offers a much earlier inference on the targeting model parameter. In this FF-2 case, the early adaptation value, 0.564 $W/m{\cdot}$K, is very close to the value inferred using the steady-state value, 0.553. Figure 17a shows the real-time inference results on all three cases. In this figure, each point represents the half-hour average value of the adapted conductivity. It can be seen that except the first half hour, the adapted value remains at a level throughout the entire simulation. Figure 17b shows the percent error compared with the end-of-experiment result. Except for the case FF-long, error remains less than 5 percent after the first half-hour. The evolution of the inferred values also indicates that it is quite possible to obtain a value of conductivity with comparable accuracy at much less time cost (10 hours Vs. 1 hour)., which could potentially greatly accelerate the experimental process.

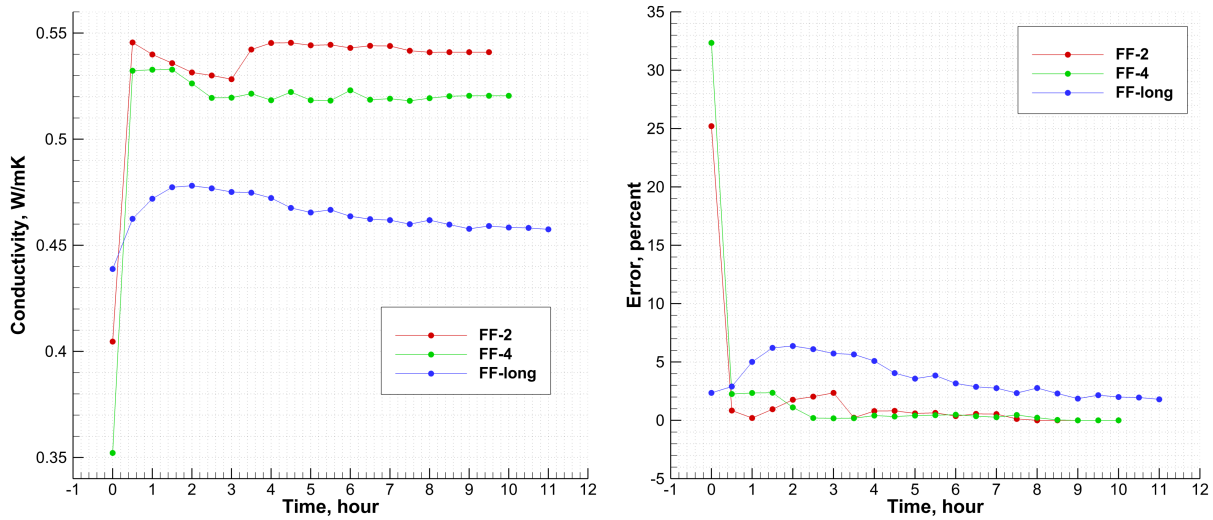

(a) Evolution of inference on conductivity

(b) Percent error compared to end-of-experiment data

Fig. 17 Real-time material property inference on three FiberForm experimental cases.

VI. Conclusion and Future Work

This work proposed a new methodology to evaluate the material property by combining the experiment and physics-based model. The demonstration test case proves that by using a data-driven approach, the parameters of a system can be revealed in a fast and accurate way. Accurate measurement of the conductivity in TPS material is of great importance. By using the retrospective adaptation algorithm, a physics-based parameter fitting methodology is achieved. The obtained conductivity is in good agreement with the experimental value and by tuning the environmental parameter, such as advection strength and contacting thermal resistance, a trustworthy range of the FiberForm conductivity is obtained. This process can also be used to better understand the experimental results and help researchers to control the most influential factors. Real-time inference is also achieved by using the on-the-run thermal couple data. The results indicate that an acceptable model parameter can be obtained in one tenth of the original experiment time cost.

For the next stage of this application, the time series of thermocouple data will be used to explore more properties, especially the material uncertainties of the FiberForm. Carbon fiber ablators, such as the ones used in TPS, have large variability in their properties. Due to the random nature of stacking or weaving fibers, those materials display a certain level of variability at different scales. The developed RCA algorithm can use the entire history of thermocouple data to match the evolution of temperature. With more richness in the data used, a more in-depth understanding of the parameters, including material variability, can be obtained.

Acknowledgments

Financial support for this work was provided by the National Science Foundation (CNS-1932105). Additional funding was provided by NASA Kentucky through NASA award No: 80NSSC20M0047, as well as through the NASA ACCESS STRI award No: 80NSSC21K1117. The authors would also like to thank the University of Kentucky Center for Computational Sciences and Information Technology Services Research Computing for their support and use of the Lipscomb Compute Cluster and associated research computing resources.

References

[1] Zhu, Y., Yi, F., Meng, S., Zhuo, L., Pan, W., and Zhang, J., "Multiphysical Behavior of a Lightweight Ablator: Experiments, Modeling, and Analysis," *Journal of Spacecraft and Rockets*, Vol. 55, No. 1, 2018, pp. 106–115. doi:10.2514/1.A33834, URL `https://doi.org/10.2514/1.A33834`.

[2] McDaniel, S., Seif, M., Fu, R., Beck, M., and Martin, A., "Development of Stochastic Model for Fibrous Ablators," *AIAA Scitech 2021 Forum*, 2021, pp. 1–11. doi:10.2514/6.2021-1473.

[3] Fu, R., McDaniel, S., Beck, M., and Martin, A., *Numerical Study of Material Uncertainties in Thermal and Structural Responses in Charring Ablation*, 2020, pp. 1–11. doi:10.2514/6.2020-0256, URL https://arc.aiaa.org/doi/abs/10.2514/6.2020-0256.

[4] Wright, M., Cozmuta, I., Laub, B., Chen, Y.-K., and Willcockson, W. H., "Defining Ablative Thermal Protection System Margins for Planetary Entry Vehicles," *42nd AIAA Thermophysics Conference*, 2011, pp. 1–11. doi:10.2514/6.2011-3757, URL https://arc.aiaa.org/doi/abs/10.2514/6.2011-3757.

[5] Gnoffo, P. A., Weilmuenster, K. J., Hamilton, K. J., Olynick, H. H., and Venkatapathy, E. V., "Computational Aerothermodynamic Design Issues for Hypersonic Vehicles," *Journal of Spacecraft and Rockets*, Vol. 36, No. 1, 1999, p. 21–43.

[6] Avco Corporation, "Ablation Handbook, Entry Materials Data and Design," Technical Report AFML-TR-66- 262, Sep 1966.

[7] Hearne, L. F., Coleman, W. D., Lefferdo, J. M., Gallagher, L. W., and Vojvodich, N. S., "A Study of the Effects of Environmental and Ablator Performance Uncertainties on Heat-Shielding Requirements for Hyperbolic Entry Vehicles," NASA CR-73224, 1968.

[8] Coleman, W. D., Hearne, L. F., Lefferdo, J. M., Gallagher, L. W., and Vojvodich, N. S., "Effects of Environmental and Ablator Performance Uncertainties on Heat-Shielding Requirements for Hyperbolic Entry Vehicles," *Journal of Spacecraft and Rockets*, Vol. 5, No. 11, 1968, pp. 1260–1270.

[9] Willcockson, W. H., "Stardust Sample Return Capsule Design Experience," *Journal of Spacecraft and Rockets*, Vol. 35, No. 3, 1999, pp. 470–474.

[10] Hoagg, J. B., and Bernstein, D. S., "Retrospective Cost Model Reference Adaptive Control for Nonminimum-Phase Systems," *Journal of Guidance, Control, and Dynamics*, Vol. 35, No. 6, 2012, pp. 1767–1786. doi:10.2514/1.57001.

[11] Rahman, Y., Xie, A., Hoagg, J. B., and Bernstein, D. S., "A Tutorial and Overview of Retrospective Cost Adaptive Control," *Proceedings of the American Control Conference*, Boston, MA, 2016, p. 3386–3409.

[12] Hoagg, J. B., and Bernstein, D. S., "Cumulative Retrospective Cost Adaptive Control with RLS-Based Optimization," *Proceedings of the American Control Conference*, Baltimore, MD, 2010, p. 4016–4021.

[13] Li, Z., Zhang, H., Bailey, S. C. C., Hoagg, J. B., and Martin, A., "A data-driven adaptive Reynolds-averaged Navier–Stokes k-ω model for turbulent flow," *Journal of Computational Physics*, Vol. 345, 2017, pp. 111–131.

[14] Li, Z., Hoagg, J. B., Martin, A., and Bailey, S. C. C., "Retrospective cost adaptive Reynolds-averaged Navier–Stokes k-ω model for data-driven unsteady turbulent simulations," *Journal of Computational Physics*, Vol. 357, 2018, pp. 353–374.

[15] Weng, H., Bailey, S. C., and Martin, A., "Numerical study of iso-Q sample geometric effects on charring ablative materials," *International Journal of Heat and Mass Transfer*, Vol. 80, 2015, pp. 570–596. doi:10.1016/j.ijheatmasstransfer.2014.09.040.

[16] Zhang, H., "High Temperature Flow Solver For Aerothermodynamics Problems," Ph.d. thesis, University of Kentucky, Lexington, KY, jul 2015. URL http://uknowledge.uky.edu/me/etds/64.

[17] Davuluri, R. S. C., Zhang, H., and Martin, A., "Numerical Study of Spallation Phenomenon in an Arc-Jet Environment," *Journal of Thermophysics and Heat Transfer*, 2015, pp. 1–10. doi:10.2514/1.T4586.

[18] Ümran Düzel, Schroeder, O. M., Zhang, H., and Martin, A., "Numerical Simulation of an Arc Jet Test Section," *Journal of Thermophysics and Heat Transfer*, Vol. 34, No. 2, 2020, pp. 393–403. doi:10.2514/1.t5722.

[19] Fu, R., Weng, H., Wenk, J. F., and Martin, A., "Thermomechanical Coupling for Charring Ablators," *Journal of Thermophysics and Heat Transfer*, Vol. 32, 2018, pp. 369–379. doi:10.2514/1.T5194.

[20] Fu, R., Weng, H., Wenk, J. F., and Martin, A., "Thermal Expansion for Charring Ablative Materials," *Journal of Thermophysics and Heat Transfer*, Vol. 52, 2019, pp. 1–9. doi:10.2514/1.t5718.

[21] Wilcox, D. C., "A complete model of turbulence revisited," *Proceedings of the 22nd Aerospace Sciences Meeting*, Reno, NV, 1984. AIAA Paper 84-0176.

[22] Ioannou, P., and Fidan, B., *Adaptive Control Tutorial, Advances in Design and Control*, Vol. 11, Society for Industrial and Applied Mathematics, Philadelphia, PA, 2006.

[23] "ASTM D5470-17, Standard Test Method for Thermal Transmission Properties of Thermally Conductive Electrical Insulation Materials," 2017. doi:10.1520/D5470-17.

[24] Barrow, C. T., Maddox, J. F., and Tagavi, K. A., "Strain-dependence of thermal conductivity in flexible fibrous insulation materials," *AIAA Scitech 2021 Forum*, 2021, pp. 1–11. doi:10.2514/6.2021-1811.